
Scalable Computing: Practice and Experience, ISSN 1895-1767, http://www.scpe.org
© 2024 SCPE. Volume 25, Issues 6, pp. 4856–4871, DOI 10.12694/scpe.v25i6.3217

DAMAGE PREDICTION EFFECT OF REINFORCED CONCRETE COLUMN AND BEAM STRUCTURE IMPROVED BY MULTIMEDIA TECHNOLOGY

YUJIAO CHEN*

Abstract. In order to improve the damage prediction effect of concrete structural column and beam structure, this paper uses multimedia technology to improve the damage prediction effect of reinforced concrete structural column and beam structure. Moreover, this paper presents the intelligent transformation model and the corresponding solution of the general damage problem, and deduces the error relationship between the result estimator and the importance function according to the error of the importance function. In addition, by analyzing the relationship between the importance function and the dual transport calculation, this paper proposes a complementary dual calculation process that can provide the importance function to each other, and builds an intelligent prediction model. Through the experimental research, it can be seen that the multimedia technology algorithm proposed in this paper can play an important role in the damage prediction of concrete structural columns and beams.

Key words: multimedia technology; reinforced concrete; structural column; beam structure; damage prediction

1. Introduction. In concrete members, due to the presence of steel bars and the influence of other bonding interfaces, creep will lead to the redistribution of stress and strain in the member, which affects the normal use and service performance of the structure. Many scholars at home and abroad have done a lot of research and analysis on the creep effect of concrete members and structures.

In the research of composite structure, the methods used to study the long-term performance of components considering creep are mainly theoretical model analysis and finite element simulation. Literature [1] proposed an effective single-step element method to analyze the long-term performance of steel-concrete composite beams, and found that the creeping effect would increase the deformation of the components and cause the phenomenon of stress redistribution, and the phenomenon of stress growth at the interface more obvious. Gilbertl4H found that under the action of creep, the ratio of the increased deflection to the initial deflection of the steel-mixed composite plate without cracking is greater than that when it is cracked. Literature [2] established a long-term effect calculation model of composite beams considering the effects of concrete shrinkage, creep and cracking, and found through research that for composite beams subjected to negative bending moments, the cracking of concrete wings will lead to a decrease in section stiffness and an increase in deflection. , while releasing the concrete stress and reducing the influence of creep effect. In the study of new and old concrete beams, the literature [3] deduces the formula of the differential stress-strain of shrinkage and creep by the mean curvature method. Literature [4] takes deformation coordination as the calculation condition, and reflects the influence of shrinkage and creep by introducing the cross-section cooperative work coefficient into the classical calculation formula of concrete structure design. Literature [5] studied the influence of shrinkage and creep effect on prestressed new and old concrete composite beams through experiments. The study showed that the concrete strain, deflection and section curvature of prestressed concrete composite beams along the beam height increased gradually with time. By studying the time-varying effect of composite beams in literature [6], it is found that the age difference between old and new concrete has no significant effect on the long-term deformation of composite beams, but it will delay the stress attenuation trend of precast slabs. In the research on concrete bridges, the literature [7] compared the prestress loss calculation methods of high-performance prestressed concrete bridges, and found the problems that were ignored in the prestress loss calculation; literature [8] analyzed the superposition through numerical software. The performance of the beam cable-stayed bridge shows that the creep has a more significant effect on the stress of the composite beam. In high-rise and super high-rise structures, literature [9] presents a consistent procedure for determining shrinkage-creep effects in reinforced

*Henan Finance University, Zhengzhou, 451464, China (Yujiao_Chen@outlook.com)

concrete building frames, considering the shearing effect of beams to evaluate elastic axial forces and axial forces due to shrinkage-creep deformation Redistribution of force. Literature [10] proposed a new method to analyze the effect of creep on reinforced concrete columns of high-rise buildings, and concluded that creep will lead to different shortening of main components and corresponding increase in bending moment.

Considering the coupling effect of concrete creep, strain energy accumulation and internal damage development under sustained load, based on statistical damage theory, Literature [11] established a concrete statistical damage model considering the coupling of creep and damage, revealing that different sustained loads the law of concrete deformation and time. Literature [12] studied the nonlinear creep characteristics of concrete under compression and its relationship with uniaxial compression damage, and proposed a physical model to explain the properties of linear and nonlinear creep strains. Failure criteria under load. Literature [13] deduces the relationship between damage degree and nonlinear creep increment through the early creep test of concrete under different stresses, and proposes a viscoelastic-plastic model to simulate the early creep of concrete. Literature [14] considered the joint effect of nonlinear viscous strain evolution and crack nucleation and propagation under high stress level, and proposed an isotropic model for concrete creep damage under uniaxial compression. The correctness of the model is verified. Literature [15] uses continuum damage mechanics to analyze the development law of concrete cracks under different stress states, and establishes the evolution equation of concrete damage development; based on concrete creep theory and strain equivalence principle, the creep damage evolution equation is established. Literature [16] proposed an orthotropic elastic-plastic damage model based on the chemical-physical mechanism, combining drying shrinkage, basic creep and drying creep models. The model distinguishes the strain components caused by the concrete's own properties and external loads, respectively, and is in good agreement with the experimental results in the short term. Literature [17] by the rheological. Combining dynamic simulation and damage mechanics, a new analytical model for predicting the response of concrete under uniaxial compression, including parameters such as creep coefficient, Poisson's ratio, and damage variables, is proposed and verified by experiments. Literature [18] established a concrete constitutive model based on continuous damage mechanics. The model considers the effect of rate correlation, and can realize the gradual degradation process of the performance of ordinary strength concrete under static load, creep and cyclic compressive loading under a unified framework. The accuracy of the model is then verified by simulation and experimental data of creep, fatigue and triaxial compression. By integrating the damage evolution equation based on the KR creep damage theory into the viscoelastic constitutive model through continuum mechanics, a viscoelastic damage model is proposed to describe the entire stage of asphalt concrete creep.

The appearance and development of concrete damage is not only due to its own characteristics and external loads, but also due to the action of ions. There have been many studies on the effect of ions on the creep of concrete. Scholars at home and abroad have also conducted some research on the creep effect of damaged concrete components caused by chloride ions under continuous load. Literature [19] conducted a time-varying reliability assessment of composite prestressed concrete box girder bridges exposed to chloride ion environment. The results show that due to the combined effect of creep, shrinkage and corrosion, the structural reliability is reduced, and the reliability indicators of the service life and the yield limit state of the steel bar are lower than the expected target levels. Literature [20] conducted experiments on the creep characteristics of concrete under the combined action of seawater erosion and compression, and studied the effects of multiple factors on the creep characteristics of concrete under seawater erosion.

The method of grid reconstruction is adopted, which involves dividing the grid into homogeneous small elements for the newly poured layer near the construction warehouse surface. As the age changes, the newly poured concrete becomes old concrete, and the homogeneous small elements are merged with the original old concrete large elements, that is, the homogeneous grid of small elements is merged into heterogeneous laminated elements. Based on the approach of grid reconstruction, virtual element or solid element degradation has been developed to construct virtual laminated element technology. At the same time, numerical analysis implementation methods have also been studied for nonlinear and creep stress calculations. Grid reconstruction technology requires the model to be re divided into units, and the process of grid connection in numerical calculations is manually adjusted, which can affect energy conservation. That is, artificially increasing or decreasing unit energy can affect calculation accuracy. Scholars have proposed another technical means to simulate the upper layer composite unit of the construction surface, namely the growth unit method, which

uses the "growth unit" to simulate the pouring process of the upper layer composite unit of the construction surface, so that the model grid can be generated in one go, Effectively solved the problem of grid reconstruction. Based on the characteristics of unit simulation in composite multi-layer materials, scholars have conducted extensive research on their layer problems, further revealing the temperature propagation and mechanical mechanism of laminated (parallel) units, providing a foundation for the application of unit simulation technology in temperature control research of large volume concrete, thin layer structure design, and other aspects. At the same time, extensive research has also been conducted on joint or crack prevention and control measures [21]. From the research and application practice of laminated elements in numerical simulation, it can be seen that the growth element method can effectively solve the problem of grid reconstruction. In the simulation of roller compacted concrete pouring construction, the added concrete layers during roller compaction construction are sequentially incorporated into the growth units as part of their physical units, achieving the "growth" and thickening of the units without increasing the number of units. Of course, due to the large number of material layers in the unit and the significant differences in material properties, it can lead to certain calculation errors. At the same time, the growth unit solves a large number of grid reconstruction problems, but the current unit incorporated into the new pouring layer has dynamic changes in node geometric coordinates and material properties. The initial calculation values after being incorporated into the new pouring layer should also be reset, and corresponding numerical techniques need to be adopted for processing [22]

The innovation of this article lies in the effective analysis of concrete structures through the use of multimedia lighting algorithms. Starting from the principles of photophysics, the existing global lighting models simulate the reflection, refraction, transmission and other behaviors of light in the scene through computer simulation, and calculate the physical and quantitative distribution of lighting energy at any point in the scene, thereby obtaining computer images with various real lighting effects.

The purpose of this article is to generate images that are as realistic as possible in the analysis of concrete structures, and to improve the reliability of concrete structure analysis in simulation

This paper uses multimedia technology to improve the damage prediction effect of reinforced concrete column and beam structure, and improves the damage prediction effect of concrete structure.

2. Improvement of multimedia intelligence algorithm. The multimedia tool models in this article include finite element simulation models, BMI models, computer-aided design, computer simulation, scientific calculation visualization, virtual display, and other tools,implementing global lighting simulation and concrete internal structure simulation through these models.

2.1. Global illumination computation based on stochastic method. The ultimate goal of the scene rendering calculation or the photorealistic image generation process is to draw the observed image of the objects in the scene for the observer (Observer) on the computer screen. The image should be consistent, or at least approximately consistent, with the real image obtained by the human eye or the camera directly observing the scene at the viewpoint.

As shown in Figure 2.1, the effect of the image (generated image and real image) seen by the observer depends on the light radiation intensity (Radiance) of each point and direction on the surface of the scene object that he receives. The illumination in the scene is generated by the light source, and the propagation of light energy in the scene and the interaction between the illumination distribution on different scene surfaces form the light radiation intensity of the scene object surface. Figure 2.2 shows the rendering process of the scene: rendering, image calculation and tone mapping.

In the global illumination system, the geometric features of the scene can be expressed by the surface model of the objects in the scene, and the general object surfaces can be expressed by mathematical surfaces or local approximate planes. The points involved in the actual calculation are some abstract points on the scene surface, as shown in Figure 2.3, and each point x has a fixed spatial coordinate and a normal vector N_x that is perpendicular to the surface outward. In addition, the differential surface element dA_x centered on x can be defined, and the spatial direction Θ represented by the differential solid angle $d\omega_\Theta$ on the unit hemisphere in the direction of N_x can be defined.

The final physical quantity solved by the global illumination calculation is the Radiant Flux (Radiant Flux) $\Phi = \frac{dQ}{dt}$, that is, the radiant energy (Q) of the light reaching or leaving the surface of the scene object per unit time, which is equivalent to the power in ordinary physics, and the unit is Watt. The radiation intensity

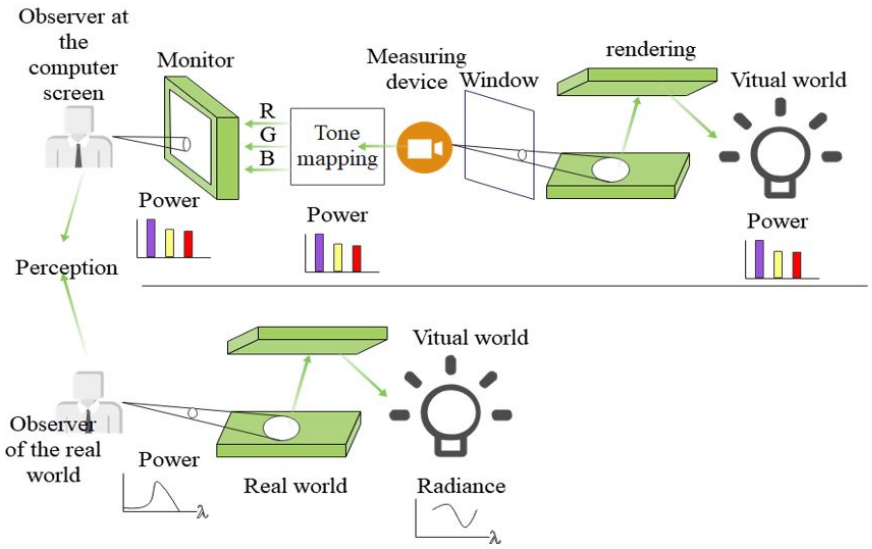

Fig. 2.1: Schematic diagram of scene renderingt

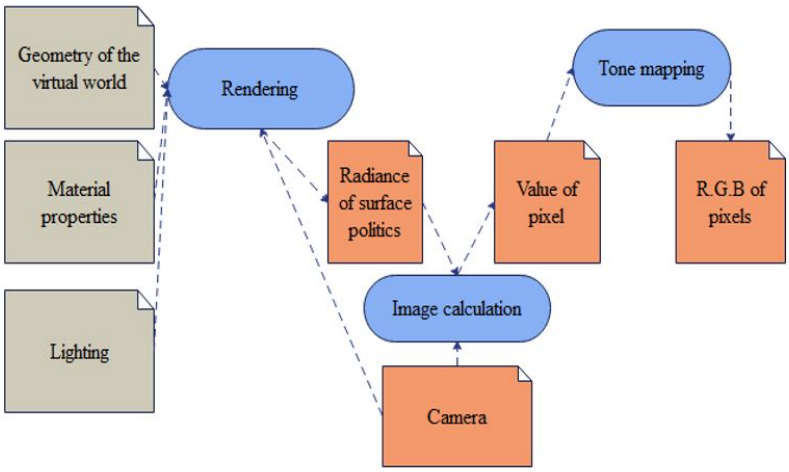

Fig. 2.2: The flow of scene rendering

$L(x, \Theta_x)$ of light arriving or leaving a certain point x on the surface of the scene object and along a certain direction Θ_x is defined as:

$$L(x, \Theta_x) = \frac{d\Phi}{dA_x^{\perp} d\omega_x} = \frac{d\Phi(x, dA_x, \Theta_x, d\omega_x)}{dA_x |\cos(N_x, \Theta_x)| d\omega_x} \tag{2.1}$$

Among them, dA_x is the area of the surface element centered at the point x, $|\cos(N_x, \Theta_x)|$ is the absolute value of the cosine of the angle between the surface normal vector N_x at the point x and the light energy propagation direction Θ_x, and $d\omega_x$ is the differential solid angle covering Θ_x. The unit of light radiation intensity is $\frac{Watt}{m^2 sr}$, and the definition domain is 5-dimensional space (3-dimensional determines the spatial position, and the other 2-dimensional determines the spatial direction). From Equation 2.1, the optical radiation flux can be calculated

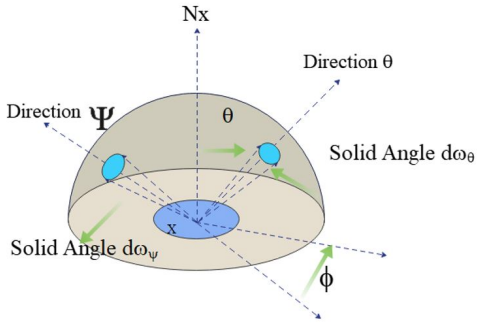

Fig. 2.3: Surface model and characterization of points in the scene

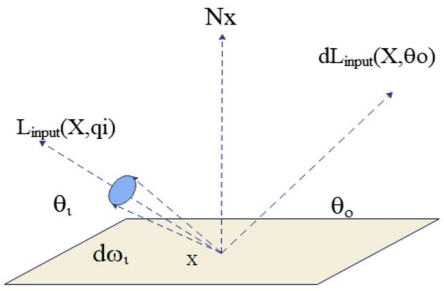

Fig. 2.4: Schematic diagram of BRDF

from the optical radiation intensity:

$$\Phi\left(A_x, \Omega_x\right) = \int_{A_x} \int_{x_x} L\left(x, \Theta_x\right) \left|\cos\left(N_x, \Theta_x\right)\right| d\omega_x dA_x. \tag{2.2}$$

The Bi-directional Reflectance Distribution Function (BRDF) is used to describe the local interaction characteristics of the surface material of the object with the light. BRDF reflects that the light energy distribution is incident on the surface of the object in a certain direction, and after the action of the surface, the molecules of the reflected light energy in the outgoing direction are shown in Figure 2.4. BRDF is often represented by f_r, and the unit is $\frac{1}{sr}$.

$$f_r\left(\Theta_i, x, \Theta_o\right) = \frac{\partial L_{\text{outpul}}\ \left(x, \Theta_o\right)}{L_{\text{input}}\ \left(x, \Theta_i\right) \left|\cos\left(N_x, \Theta_i\right)\right| \partial\omega_{in}} = \frac{dL_{\text{ouput}}\ \left(x, \Theta_o\right)}{L_{\text{input}}\ \left(x, \Theta_i\right) \left|\cos\left(N_x, \Theta_i\right)\right| d\omega_{\text{in}}} \tag{2.3}$$

Among them, $L_{\text{output}}\ \left(x, \Theta_o\right)$ is the reflected light radiation intensity at point x along direction Θ_o, $L_{\text{input}}\ \left(x, \Theta_i\right)$ is the light radiation intensity incident at point x along direction Θ_i, and $d\omega_{in}$ is the differential solid angle covering Θ_i.

The light measuring device is characterized by the light sensitivity function $W_e\left(x, \Theta_x\right)$. The definition domain of the light sensitive function $W_e\left(x, \Theta_x\right)$ is the set of certain points x on the surface of the scene object within a certain range and its corresponding set of certain directions Θ_x that form a solid angle Ω_x that covers a certain direction in three-dimensional space. The set of points A_x and the set of directions Ω_x are collectively referred to as the phase space S defined by the light sensitivity function, namely $S = \left(A_x, \Omega_x\right)$.

The light sensitivity function can be defined as follows:

$$W_e\left(x, \Theta_x\right) = \begin{cases} C\left(x, \Theta_x\right) \in S \\ 0\left(x, \Theta_x\right) \in S \end{cases} \tag{2.4}$$

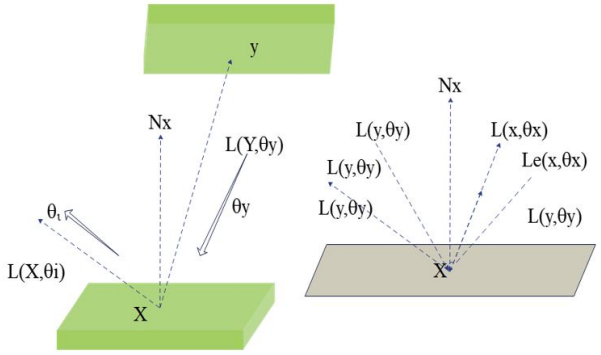

Fig. 2.5: Schematic diagram of the radiance equation

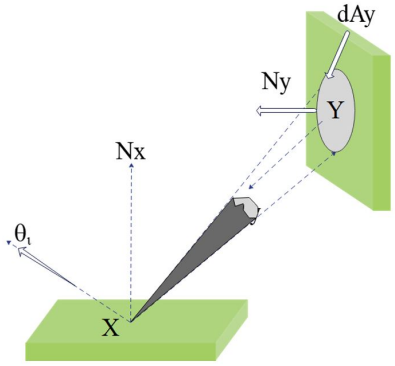

Fig. 2.6: Schematic diagram of rendering equations

$W_e(x, \Theta_x)$ provides a constant value C for the independent variable within its scope of action (that is, the set of points and corresponding directions), and the function value outside its scope of action is always zero. In this way, the illumination measurement value that can be obtained by measuring the illumination distribution of the scene by the illumination measuring device with $W_e(x, \Theta_x)$ as the illumination sensitivity function is:

$$\begin{aligned} M(S) &= \int_{A_x} \int_{h_x} d\Phi(x, dA_x, \Theta_x, d\omega_x) W_e(x, \Theta_x) \\ &= \int_{A_x} \int_{\Omega_x} L(x, \Theta_x) |\cos(N_x, \Theta_x)| W_e(x, \Theta_x) d\omega_x dA_x \end{aligned} \tag{2.5}$$

The light radiation intensity equation is defined as follows:

$$L(x, \Theta_x) = L_e(x, \Theta_x) + \int_{h_{x/h}} L(y, \Theta_y) f_r(\Theta_y, x, \Theta_x) |\cos(N_x, \Theta_y)| d\omega_y \tag{2.6}$$

As shown in Figure 2.5, the equation represents that the light radiation intensity $L(x, \Theta_x)$ of a point x on the surface of the scene object along a direction Θ_x is equal to the luminous optical radiation intensity $L_e(x, \Theta_x)$ of the point in this directions and the sum of all the optical radiation intensity $L(x, \Theta_x)$ incident to the point along the hemispherical direction of the x point and reflected to the Θ_x direction.

As shown in Figure 2.6, according to the definition of solid angle, by transforming the differential solid angle in the light radiation intensity equation, the drawing equation can be obtained:

$$\begin{aligned} &L(x, \Theta_x) = L_e(x, \Theta_x) + \\ &\int_{A_y} L(y, \Theta_y) f_r(\Theta_y, x, \Theta_x) V(x, y) |\cos(N_x, \Theta_y)| \frac{|\cos(N_y, \Theta_y)|}{|y-x|^2} dA_y \end{aligned} \tag{2.7}$$

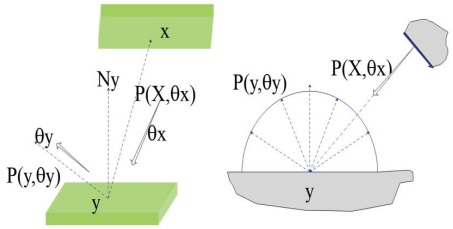

Fig. 2.7: Schematic diagram of potential energy equation

Among them, V(x,y) is the visibility function. It takes the value 1 when point x and point y are visible to each other, and 0 otherwise. Both the light radiation intensity equation and the drawing equation are mathematically recursive integral equations, namely the second Fredhlom integral equation. Such integral equations generally have no analytical (exact) solution.

This is especially true for the complex integral equation describing the light energy transport in the field of global illumination computing, which can only be solved by numerical calculation methods.

From the definition of the light sensitivity function $W_e(x, \Theta_x)$ (equation (4)), the measured value of light (equation (2.5)) is:

$$M(S) = \int_1 \int_\Omega L(x, \Theta_x) \left|\cos(N_x, \Theta_x)\right| W_e(x, \Theta_x) \, d\omega dA \tag{2.8}$$

Among them, A represents the surface area of the entire scene, and Ω represents all the spatial directions. Equation (2.2) is rewritten as:

$$\Phi(S) = \int_{A_x} \int_x L(x, \Theta_x) \left|\cos(N_x, \Theta_x)\right| P_e(x, \Theta_x) \, d\omega_x dA_x. \tag{2.9}$$

Here $S = (A_x, \Omega_x)$ is the set of points and corresponding directions. If $P_e(x, \Theta_x) = \frac{W_e(x, \Theta_x)}{C}$ is defined, then there is:

$$P_e(x, \Theta_x) = \begin{cases} 1 \, (x, \Theta_x) \in S \\ 0 \, (x, \Theta_x) \in S \end{cases} \tag{2.10}$$

Among them, $P_e(x, \Theta_x)$ is the potential energy function, indicating whether the light radiation intensity $L(x, \Theta_x)$ contributes to the light radiation flux flowing through the set S and the size of the contribution. The potential energy function $P(x, \Theta_x)$ of the point x along the direction Θ_x with respect to the set S is defined as:

$$P(x, \Theta_x) = \frac{d^2\Phi(S)}{d^2\Phi_e(x, A_x, \Theta_x, \Omega_x)} = \frac{d^2\Phi(S)}{L_e(x, \Theta_x) \left|\cos(N_x, \Theta_x)\right| d\omega_x dA_x} \tag{2.11}$$

$P(x, \Theta_x)$ gives the ratio of the (differential) optical radiant flux flowing through the set S to the (differential) optical radiant flux emitted by the light source. Its size is only related to the geometry of the objects contained in the scene and the optical properties of the materials on the surfaces of the objects.

According to the definition of potential energy function, we can get:

$$\Phi(S) = \int_{A_x} \int_{\lambda_x} L_e(x, \Theta_x) \, P(x, \Theta_x) \left|\cos(N_x, \Theta_x)\right| d\omega_x dA_x \tag{2.12}$$

Similar to the intensity of light radiation, the potential energy function also satisfies a second kind of Fredhlom integral equation, called the potential energy equation. As shown in Figure 2.7, when a point and

corresponding direction set S are given, the potential energy function $P(x, \Theta_x)$ of a point x on the scene object surface along the direction Θ_x with respect to this set S consists of two parts, namely the direct contribution part and the indirect contribution part. Among them, the direct contribution part is expressed by $P_e(x, \Theta_x)$, and the indirect contribution part $L(x, \Theta_x)$ is the contribution of the scene surface point y that can directly act on, that is, the sum of the contributions of all $L(y, \Theta_y)$ on the hemisphere to the set S through $f_r(\Theta_x, y, \Theta_y)$. From this, the potential energy equation can be written as:

$$P(x, \Theta_x) = P_e(x, \Theta_x) + \int_{h_y} P(y, \Theta_y) f_r(\Theta_x, y, \Theta_y) |\cos(N_y, \Theta_y)| d\omega_y \tag{2.13}$$

If $W(x, \Theta_x) = P(x, \Theta_x) * C$, by equation (2.13), we can get:

$$W(x, \Theta_x) = W_e(x, \Theta_x) + \int_{h_y} W(y, \Theta_y) f_r(\Theta_x, y, \Theta_y) |\cos(N_y, \Theta_y)| d\omega_y \tag{2.14}$$

Equation (2.14) is also often referred to as the potential energy equation, and $W(x, \Theta_x)$ can also be considered as a more abstract, general light sensitivity function. In this way, the measured value of the scene lighting distribution can be written as:

$$M(S) = \int_{A_x} \int_{h_x} L_e(x, \Theta_x) |\cos(N_x, \Theta_x)| W(x, \Theta_x) d\omega_x dA_x \tag{2.15}$$

Undoubtedly, the potential energy equation and the corresponding illumination measurement equation (equations 2.14 and (2.15)) also completely define the global illumination calculation problem. Moreover, solving the potential energy equation and its corresponding illumination measurement equation also provides a computational approach for us to solve the global illumination calculation problem.

The two basic equationtions of the global illumination computational problem, the rendering/light radiation intensity equation and the potential energy equation, have the same integral form mathematically, and can be represented by a more general transport equation. Transport equations also have their corresponding integral equations of measurement, which constitute the description of transport problems in general. The operators $(K)(\bullet)$ and $\langle \bullet, \bullet \rangle$ are defined as follows:

$$(Kf)(x) = \int K(x, x_1) f(x_1) dx_1$$

$\langle g(x), f(x) \rangle = \int f(x) g(x) dx$. Then, the transportation problem can be expressed as:

$$\Phi(x) = K\Phi(x) + \sigma(x) = \int_{\alpha} K(x, x_1) \Phi(x_1) dx_1 + \sigma(x) \tag{2.16}$$

$$I = \langle g(x), \Phi(x) \rangle = \int \Phi(x) g(x) dx \tag{2.17}$$

Among them, the function $\Psi(x)$ is the unknown quantity to be solved, and $\sigma(x)$ is the value of $\Phi(x)$ under certain conditions, which is called the source function and a known quantity. $K(x, x_1)$ is called the kernel function, which represents a certain interdependence between the distributions $\Phi(x)$ and $\Phi(x_1)$ of the function $\Phi(x)$ at two points xx_1 in the phase space. The ultimate purpose of solving the transport problem is to obtain the integral value I given by equation (2.17), where g(x) is called the response function.

$$\Phi = K\Phi + \sigma \tag{2.18}$$

If there is an integral operator $K^*(\bullet)$

$$(K^* f)(x) = \int K^*(x, x_1) f(x_1) dx_1$$

and the corresponding transport equation

$$\Phi^* = K^*\Phi^* + \sigma^* = K^*\Phi^* + g = \int K^*(x, x_1)\,\Phi^*(x_1)\,dx_1 + g(x) \tag{2.19}$$

Make

$$\langle K^*\Phi^*, \Phi\rangle = \langle \Phi^*, K\Phi\rangle \tag{2.20}$$

is established, then the integral operator $K^*(\bullet)$ is called the adjoint operator of the adjoint operator. The transport equation (Equation (2.19)) is the Duality or Adjoint of the transport equation (Equation (2.16)/Equation (2.18)). In this way, the integral equation of the transportation problem (such as equation (17)) can be written as:

$$I = \langle \sigma, \Phi^*\rangle = \int \Phi^*(x)\sigma(x)dx \tag{2.21}$$

Then, the transport problems defined by equations (2.19) and (2.21) are dual or adjoint in the mathematical sense of the transport problems defined by equations (2.16) and (2.17). Obviously, the potential energy equation (2.14) and the equation (2.15) are the dual/adjoint in the mathematical sense of the light radiation intensity equation (equation (6)), and they describe the global illumination calculation problem from two different angles. The global illumination problem can start from these two different ways and get the same answer.

The drawing equation (equation (7)) can be expanded as:

$$L = L_e + TL_e + T^2L_e + \cdots + T^nL_e + \cdots$$

The integral operators $(Tf)(\bullet)$ and $(T^*f)(\bullet)$ involved in the global illumination calculation problem are both compact operators, namely $T \leq 1$, then there is $\lim_{n\to\infty} T^{n+1}L = 0$, that is, the series obtained by L expansion converges. Therefore, we end up with:

$$L = \sum_{i=0}^{\infty} T^iL_e \tag{2.22}$$

The light measurements is:

$$M = \langle L, W_e\cos\theta\rangle = \left\langle \sum_{i=0}^{\infty} T'L_e, W_e\cos\theta \right\rangle \tag{2.23}$$

It can be seen that the infinite expansions (equations (2.22) and (2.23)) of light radiant intensity and its corresponding illumination measurements are the sum of a series (up to infinity) of high-dimensional integrals of increasing (up to infinite) dimensions. Mathematically, it is called the Newman sequence. Similarly, the potential energy equation and its light measurement equation can also be expanded into the corresponding sequence form.

2.2. Monte CarIo method. The desire point is:

$$I = \int_{\lambda_x} f(x)dx \tag{2.24}$$

Among them, $x = x(y_1, \cdots, y_s)$ represents a point in the s-dimensional space of the integration area, and the function f(x) belongs to the L^2 function space. We take any probability density function (PDF) on Ω_s:

$$p(x)\,(p(x) \neq 0\,(x \in \Omega_s \text{ and } f(x) \neq 0)), \text{ order } g(x) = \begin{cases} \frac{f(x)}{p(x)}f(x) \neq 0 \\ 0f(x) = 0, \end{cases}$$

The equation (2.1) can be rewritten as:

$$I = \int_{\lambda_s} g(x)p(x)dx = E[g(x)] \tag{2.25}$$

That is, the integral I to be found is the mathematical expectation of the random variable g(x), and the probability density function obeyed by the independent variable x is p(x). If N samples$x_i (1 \leq i \leq N)$ of random variable x are drawn according to p(x), then the arithmetic mean is:

$$\hat{I}_N = \frac{1}{N} \sum_{i=1}^{N} g\left(x_i\right) \tag{2.26}$$

That is, an approximate estimate of the integral I. g(x) is the primary estimator (PrimaryEstimator) of the integral I, and $\bar{I}_N$ (where x_i is an arbitrary variable) is the secondary estimator of the integral I.

If there is a random variable Y, and its mathematical expectation is I^*, that is, $E[Y] = I^*$, then Y is an unbiased estimate of g, otherwise Y is a biased estimate of I^*. It is easy to see that the above g(x) and $\frac{1}{N} \sum_{i=1}^{N} g\left(x_i\right)$ are both unbiased estimates of I to be found.

Th Law of Large Numbers enhanced by Kolmogorov can guarantee the convergence of MonteCarlo calculation integral, and the error order of the calculation result is $O\left(N^{-1/2}\right)$.

Considering the calculation of the definite integral I (equation (24)), we take any joint probability density function $p_1(x)$ on the integral region Ω_s and $p_1(x)$ satisfies the conditions: $p_1(x) \neq 0 \, (x \in \Omega_s$ and $g(x)p(x) \neq 0)$. If $g_1(x) = g(x)W(x) \neq 0$ and $W(x) = \begin{cases} \frac{p(x)}{p_1(x)} & p_1(x) \neq 0 \\ 0 & p_1(x) = 0 \end{cases}$ then $I = \int_{\Omega_s} g_1(x)p_1(x)dx = E\left[g_1(x)\right]$. Sampling N sample points $x_i (1 \leq i \leq N)$ from $p_1(x)$, we can get:

$$\hat{I}_{1N} = \frac{1}{N} \sum_{i=1}^{N} g_1\left(x_i\right) \tag{2.27}$$

Obviously, $\hat{I}_{1N}$ is an unbiased estimate of I. Traditionally, sampling from distribution $p_1(x)$ is called offset sampling from distribution p(x), and the factor W(x) is called weighting factor to correct the skewness caused by sampling from distribution $p_1(x)$. According to the importance sampling theory, the optimal $p_1(x)$ is obtained, that is, $p^*(x)$ makes the variance ${\sigma_{g_1}}^2$ of the estimator g_1 zero, where $p^*(x) = \frac{|g(x)|p(x)}{\int_{3_s} |g(x)|p(x)dx}$. When $g(x) \geq 0$, there is:

$$p^*(x) = \frac{g(x)p(x)}{\int_{h_x} g(x)p(x)dx} = \frac{g(x)p(x)}{I} \tag{2.28}$$

Here, the function $|g(x)|(g(x))$ is called the importance function.

To compute the integral $I = \int_2 f(x)dx = \int_{h_r} g(x)p(x)dx$, where p(x) is the probability density function, then g(x) is an unbiased estimator of I. If there is a positive decimal q (0<q<1), and $I_q = \int_2 \frac{1}{q} f(x)dx = \int_\Omega \frac{g(x)}{q} p(x)dx$, then $I = q \cdot I_q + (1-q) \cdot 0$. In this way, the integral I to be obtained is the mathematical expectation of a random variable ζ with a two-point probability distribution, where the characteristic of ζ is $P\left\{\zeta = I_q\right\} = q, P\{\zeta = 0\} = 1 - q$. The positive decimal q is just treated as a probability value. Therefore, the integral I can be obtained by simulating the two-point probability distribution model, which is the Russian Roulette technique. Russian roulette provides an unbiased termination mechanism for the calculation of infinite-dimensional integrals, which makes the calculation terminate in finite steps while ensuring the unbiased estimated value of the result.

2.3. General model of Monte Carlo method for global illumination problem. The global illumination calculation problem can be reduced to a general transport problem:

$$\Phi(x) = \int K\left(x, x_1\right) \Phi\left(x_1\right) dx_1 + \sigma(x) \tag{2.29}$$

$$I = \int \Phi(x) g(x) dx \tag{2.30}$$

The general way to calculate the integral I defined by equation (2.30) using the MonteCarlo method is: If the normalization $G(x) = \frac{g(x)}{\int g(x)dx}$ of the function g(x) is known in this equation as the probability density function, and N sample points $x_i (1 \leq i \leq N)$ are randomly sampled, then an unbiased estimate of the integral I is:

$$\hat{I}_N = \left(\int g(x) dx \right) \frac{1}{N} \sum_{i=1}^{N} \Phi(x_i) \tag{2.31}$$

Since $\Phi(x)$ is unknown, equation (2.29) must be solved to obtain $\Phi(x_i)$.

For any $\Phi(x_i)$, the method of using the random walk technique to obtain its estimated value $\langle \Phi(x_i) \rangle$ is: by sampling N random sample points $y_j (1 \leq i \leq N)$, we can get:

$$\langle \Phi(x_i) \rangle = \sigma(x_i) + \frac{1}{N} \sum_{j=1}^{N} \frac{K(x_i, y_j) \Phi(y_j)}{p_1(y_j)} \tag{2.32}$$

Repeating the above MonteCarlo integration process, we can get:

$$\begin{aligned} &\langle \Phi(x_i) \rangle = \sigma(x_i) + \frac{1}{N_1} \sum_{j=1}^{N_1} \frac{K(x_i, y_j)}{p_1(y_j)} \left[\sigma(y_j) + \frac{1}{N_2} \sum_{k=1}^{N_2} \frac{K(y_j, z_k)}{p_2(z_k|y_j)} \Phi(z_k) \right] \\ &= \sigma(x_i) + \frac{1}{N_1} \sum_{j=1}^{N_1} \frac{K(x_i, y_j)}{p_1(y_j)} \left[\sigma(y_j) + \frac{1}{N_2} \sum_{k=1}^{N_2} \frac{K(y_j, z_k)}{p_2(z_k|y_j)} (\sigma(z_k) + \cdots) \right] \end{aligned}$$

The conditional probability density function $p_2(z_k|y_j)$ is actually the transition probability density function from the random state y_j to the random state z_k. In order to reduce the geometrical increase of the computational complexity due to the huge number of sampling points generated by each sampling, each MonteCarlo integration only uses one random sample point, which forms the so-called random walk chain. An estimate can be obtained by simulating a random walk chain:

$$\langle \Phi(x_i) \rangle = \sigma(x_i) + \frac{K(x_i, y_1)}{p_1(y_1)} \sigma(y_1) + \frac{K(x_i, y_1)}{p_1(y_1)} \frac{K(y_1, y_2)}{p_2(y_2|y_1)} \sigma(y_2) + \cdots \tag{2.33}$$

The random variable sequence $\{y_j | j = 1, 2, \cdots, N, \cdots)\}$ in equation (2.32) constitutes a random walk chain.

In order to ensure the feasibility of the calculation, the random walk chain cannot go on indefinitely, and Russian roulette can introduce a termination mechanism for the generation of the random walk chain. Before proceeding to the next sampling, the survival probability determines whether to establish the next random state, so that the process will always stop at a random state. From this, the estimate of the solution to the integral equation is the sum of the finite terms:

$$\begin{aligned} &\langle \Phi(x_i) \rangle = \sigma(x_i) + \frac{K(x_i, y_1)}{P_1 \cdot p_1(y_1)} \sigma(y_1) + \frac{K(x_i, y_1)}{P_1 \cdot p_1(y_1)} \frac{K(y_1, y_2)}{P_2 \cdot p_2(y_2|y_1)} \sigma(y_2) + \cdots \\ &+ \frac{K(x_i, y_1)}{P_1 \cdot p_1(y_1)} \frac{K(y_1, y_2)}{P_2 \cdot p_2(y_2|y_1)} \cdots \frac{K(y_{k-1}, y_k)}{P_k \cdot p_k(y_k|y_{k-1})} \sigma(y_k) \end{aligned} \tag{2.34}$$

Among them, $P_j (j = 1, 2, \cdots, k)$ is the survival probability $P_j (j = 1, 2, \cdots, k)$. If the kernel function $K(x, x_1)$ is used as the state transition probability density function between random states, because the normalized value of the kernel function in practical application problems is often less than 1 (this is the case in the global illumination calculation problem), that is, $\int K(x, x_1) dx_1 < 1$, then the correct state transition probability density function between random states is the normalized kernel function:

$$p_k(y_k|y_{k-1}) = \frac{K(y_{k-1}, y_k)}{\int K(y_{k-1}, y_k) dy_k}, \text{ here } y_0 = x_i \tag{2.35}$$

Moreover, the normalized value of the kernel function is the probability of survival in Russian roulette.

$$P_k = \int K(y_{k-1}, y_k) dy \tag{2.36}$$

Finally, an estimate of the solution to the integral equation in a very simplified form can be obtained:

$$\langle \Phi (x_i) \rangle = \sum_{j=0}^{k} \sigma (y_j) \tag{2.37}$$

The estimated value given by equation (2.37) is the so-called critical estimated value. The kernel function whose normalized value is less than 1 is often called the sub-critical probability density function

Generally, multiple random walk chains are used to solve the integral equation to reduce the variance. The estimated value of the equation solution is the average value of the contributions of all random walk chains, namely:

$$\langle \Phi (x_i) \rangle = \frac{1}{n_{\text{walks}}} \sum_{j=1}^{n_{\text{watk}}} \left[\sigma (x_i) + \frac{K (x_i, y_1)}{p_1 (y_1)} \sigma (y_1) + \frac{K (x_i, y_1)}{p_1 (y_1)} \frac{K (y_1, y_2)}{p_2 (y_2 y_1)} \sigma (y_2) + \cdots \right] \tag{2.38}$$

It can be seen that the current MonteCarlo global illumination algorithm is based on two parts: a random sampling process for MonteCarlo integral calculation and a random walk simulation process for solving the second type of Fredholm integral equation.

According to the reproducibility sampling principle of the new computational model, the unknown function $\Phi(x)$ in the original transport problem is the importance function for solving the dual transport problem. Conversely, the unknown function $\Phi(x)$ in the dual transport problem is the importance function for solving the original transport problem. In this way, the initial probability density, intermediate probability density and termination probability of the importance random sampling for solving the transport problem are:

$$p^* (x_0) = \frac{\Phi (x_0) g (x_0)}{\int \Phi (x_0) g (x_0) dx_0} \tag{2.39}$$

$$p^* (x_i, x_{i-1}) = \frac{K (x_{i-1}, x_i) \Phi (x_i)}{\Phi (x_{i-1})} \tag{2.40}$$

$$q^* (x_L) = \frac{\sigma (x_L)}{\Phi (x_L)} \tag{2.41}$$

At this point, the variance of the termination estimator $\langle I \rangle_T^*$ is zero, namely $Var \left[\langle \rangle^\circ \tau \right] = 0$, where:

$$\langle I \rangle^* = \frac{\sigma (x_L)}{q^* (x_L)} \frac{K (x_{L-1}, x_L) \cdots K (x_0, x_1)}{p^* (x_L, x_{L-1}) \cdots p^* (x_1, x_0)} \frac{g (x_0)}{p^* (x_0)} \tag{2.42}$$

According to the corresponding relationship between the dual global illumination calculation problem and the dual transport problem and the corresponding relationship between the original global illumination calculation problem and the original transport problem, and the definitions of equations (2.39) to (2.41), the initial probability density, intermediate probability density and termination probability of the optimized potential energy tracking can be obtained:

$$p^* (x_0, \Theta_{x_0}) = \frac{W_e (x_0, \Theta_{x_0}) \left| \cos (N_{x_0}, \Theta_{x_0}) \right| L (x_0, \Theta_{x_0})}{\int_{x_{x_0}} \int_{2_{x_0}} W_e (x_0, \Theta_{x_0}) \left| \cos (N_{x_n}, \Theta_{x_0}) \right| L (x_0, \Theta_{x_0}) dA_{x_0} d\omega_{x_0}} \tag{2.43}$$

$$p^* \left[(x_i, \Theta_{x_i}), (x_{i-1}, \Theta_{x_{i-1}}) \right] = \frac{f_r \left(\Theta_{x_i}, x_{i-1}, \Theta_{x_{t-1}} \right) \left| \cos \left(N_{x_{t-1}}, \Theta_{x_i} \right) \right| L (x_i, \Theta_{x_1})}{L \left(x_{i-1}, \Theta_{x_{i-1}} \right)} \tag{2.44}$$

$$q^* (x_L, \Theta_{x_L}) = \frac{L_e (x_L, \Theta_{x_L})}{L (x_L, \Theta_{x_L})} \tag{2.45}$$

The zero-variance termination estimator $PT_T{}^*$ calculated by the optimized potential energy tracking algorithm to calculate the light measurement estimates is:

$$PT_T^* = \frac{f_r\left(\Theta_{x_L}, x_{L-1}, \Theta_{x_{L-1}}\right)\left|\cos\left(N_{x_{L-1}}, \Theta_{x_L}\right)\right|_{x^*}}{p^*\left[\left(x_L, \Theta_{x_L}\right), \left(x_{L-1}, \Theta_{x_{L-1}}\right)\right]} \times \frac{f_r\left(\Theta_{x_1}, x_0, \Theta_{x_0}\right)\left|\cos\left(N_{x_n}, \Theta_{x_1}\right)\right|}{p^*\left[\left(x_1, \Theta_{x_1}\right), \left(x_0, \Theta_{x_0}\right)\right]} \times \frac{W_e\left(x_0, \Theta_{x_0}\right)\left|\cos\left(N_{x_0}, \Theta_{x_0}\right)\right|}{p^*\left(x_0, \Theta_{x_0}\right)} \times \frac{L_e\left(x_L, \Theta_{x_L}\right)}{q^*\left(x_L, \Theta_{x_L}\right)} \tag{2.46}$$

The light radiation intensity function $L\left(x_{i-1}, \Theta_{x_{i-1}}\right)$ with the right-hand side of the equal sign in equation (2.44) on the denominator is the normalization factor, and the light radiation intensity functions $L\left(x_0, \Theta_{x_0}\right)$ and $L\left(x_i, \Theta_{x_i}\right)$ on the numerator on the right-hand side of the equation (2.43) and (2.45) are the importance functions.

3. Using multimedia technology to improve damage prediction effect of reinforced concrete column and beam structure. On the basis of the right-hand coordinate system rule, the overall cylindrical coordinate system adopts the 0-axis: Z coordinate system. Set the positive direction of the Z-axis as the vertical outward direction of the tunnel, the center of the circle with a vertical coordinate of 0 as the origin of the coordinate axis, the T-axis as the tangential direction of the tunnel, and the R-axis as the radial direction of the tunnel. Multimedia concrete models typically include soil foundations, pipe segments, prestressed steel bars, and concrete structures, taking into account the combined effects between external surrounding rock, prestressed concrete inner lining, and shield tunneling pipe segment outer lining. Modeling the reinforced concrete lining and prestressed tendons separately, considering the influence of curved prestressed tendons on concrete, so that the constructed multimedia concrete model can accurately simulate the internal force distribution of concrete lining structures affected by the curve shape of prestressed tendons. Discretize the lining structure and soil structure according to three-dimensional solid elements, and discretize the prestressed steel strands according to 2-node rod elements to construct a multimedia concrete model for concrete lining.

To improve the stress calculation accuracy of the cushion multimedia model, data such as the deformation at both ends and the temperature difference of the steel plate during pressure transmission and relative closure during operation were obtained through simulation calculation. After densifying the grid, the stress of the steel pipe was calculated using the plate shell finite element method.

As shown in Figure 3.1, the following figure is two images selected from the concrete CT image data set. It can be intuitively seen that the images contain a large number of holes and small objects, and they have the characteristics of high density and small distance between each other. Due to the small area occupied by a single hole, very little feature information is extracted after entering the convolutional neural network, which leads to a low accuracy of the detection model. Therefore, there are high challenges in the internal damage detection of concrete CT images. The method in this paper is used for research.

Figure 3.2 shows the concrete output image recognized by multimedia technology, which verifies the reliability of the method proposed in this paper. On this basis, the performance of the method in this paper in the damage prediction of concrete structural columns and beams is evaluated through multiple sets of experiments.Comparing the method proposed in this article with the model proposed in reference [10], the experimental results are shown in Table 3.1.

Propose a multimedia based simulation technology for concrete lining structures, which can reliably simulate the stress of concrete structures. It can effectively calculate the peak stress of lining concrete, shield tunnel lining segments, and steel strands, accurately analyze the stress of concrete lining structures, and lay a foundation for the application and development of concrete lining structures

By improving the accuracy of prediction, the analysis effect of concrete structures can be improved, and the design and actual construction effects can be improved, thereby enhancing the safety and reliability of concrete structures

It can be seen from the above research that the multimedia technology algorithm proposed in this paper can play an important role in the damage prediction of concrete structural columns and beams.

4. Conclusion. The internal damage and macroscopic damage of concrete have been widely concerned by experts and scholars at home and abroad. However, most of them use computed tomography technology to scan the loaded concrete structure to generate two-dimensional tomographic sequence images, and use CT images

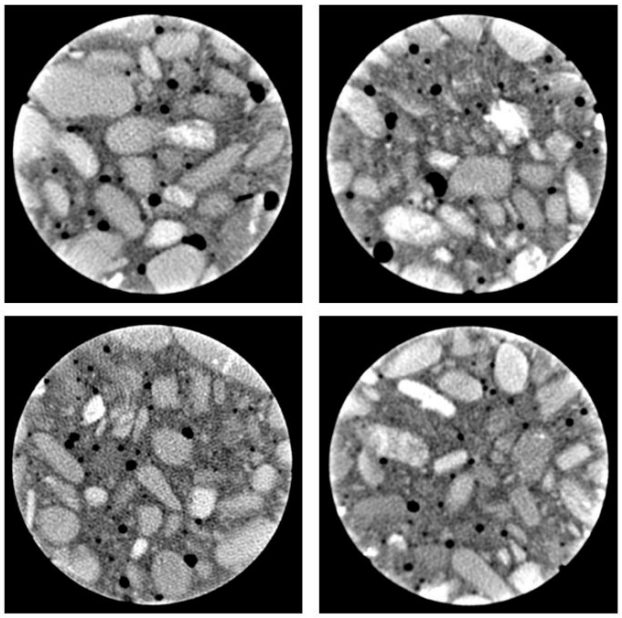

Fig. 3.1: CT image of concrete used in this paper

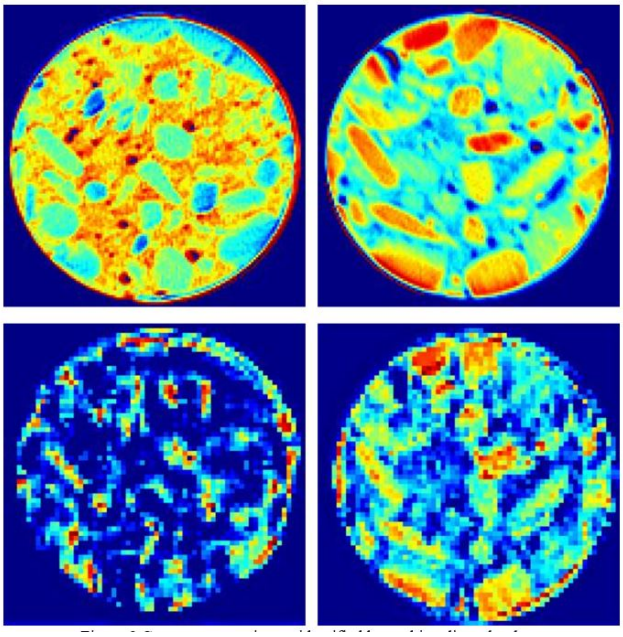

Fig. 3.2: Concrete output image identified by multimedia technology

to conduct static analysis and dynamic simulation to study the internal structure of concrete. Concrete CT images often have many noises and large artifacts, which greatly affects the research results of concrete meso-damage. The rise of deep learning has provided a new solution for the study of the internal damage structure of concrete. This paper uses multimedia technology to improve the damage prediction effect of reinforced concrete

Table 3.1: Damage prediction effect of concrete column and beam structure

Num	The method of this article	The method of reference [10]	Num	The method of this article	The method of reference [10]
1	89.79	80.47	11	91.79	79.18
2	87.67	87.21	12	91.41	83.22
3	91.73	81.54	13	90.31	82.68
4	91.48	85.33	14	90.31	83.10
5	88.26	83.78	15	87.22	84.94
6	89.25	87.32	16	88.37	86.47
7	89.73	81.41	17	89.12	87.62
8	88.79	86.66	18	88.55	79.84
9	87.68	82.65	19	91.79	85.78
10	87.14	79.63	20	90.27	79.44

column and beam structure, and improves the damage prediction effect of concrete structure. Through the experimental research, it can be seen that the multimedia technology algorithm proposed in this paper can play an important role in the damage prediction of concrete structural columns and beams.

Propose a simulation method for the internal structure of concrete based on multimedia models, which can effectively calculate the peak stress of lining concrete, shield tunnel lining segment stress, and steel strand stress, accurately analyze the stress of concrete lining structures, and lay the foundation for the application and development of concrete lining structures. Subsequent research will verify the model in this paper through multiple sets of practical engineering

REFERENCES

[1] Beckmann, B., Bielak, J., Bosbach, S., Scheerer, S., Schmidt, C., Hegger, J. & Curbach, M. Collaborative research on carbon reinforced concrete structures in the CRC/TRR 280 project. *Civil Engineering Design*. **3**, 99-109 (2021)

[2] Jo, J., Jo, B., Cho, W. & Kim, J. Development of a 3D printer for concrete structures: laboratory testing of cementitious materials. *International Journal Of Concrete Structures And Materials*. **14**, 1-11 (2020)

[3] Burger, J., Lloret-Fritschi, E., Scotto, F., Demoulin, T., Gebhard, L., Mata-Falcón, J. & Flatt, R. Eggshell: ultra-thin three-dimensional printed formwork for concrete structures. *3D Printing And Additive Manufacturing*. **7**, 48-59 (2020)

[4] Yang, S., Gu, X., A, X. & Zhang, Q. Explosion damage analysis of concrete structure with bond-associated non-ordinary state-based peridynamics. *Engineering With Computers*. **39**, 607-624 (2023)

[5] Tošić, N., Torrenti, J., Sedran, T. & Ignjatović, I. Toward a codified design of recycled aggregate concrete structures: Background for the new fib Model Code 2020 and Eurocode 2. *Structural Concrete*. **22**, 2916-2938 (2021)

[6] Mishra, M., Jain, V., Singh, S. & Maity, D. Two-stage method based on the you only look once framework and image segmentation for crack detection in concrete structures. *Architecture, Structures And Construction*. **3**, 429-446 (2023)

[7] Figueira, R., Almeida, J., Ferreira, B., Coelho, L. & Silva, C. Optical fiber sensors based on sol–gel materials: design, fabrication and application in concrete structures. *Materials Advances*. **2**, 7237-7276 (2021)

[8] Baharuddin, N., Nazri, F., Bakar, B., Beddu, S. & Tayeh, B. Potential use of ultra high-performance fibre-reinforced concrete as a repair material for fire-damaged concrete in terms of bond strength. *International Journal Of Integrated Engineering*. **12**, 87-95 (2020)

[9] Slobbe, A., Rozsas, A., Allaix, D. & Bigaj-van Vliet, A. On the value of a reliability-based nonlinear finite element analysis approach in the assessment of concrete structures. *Structural Concrete*. **21**, 32-47 (2020)

[10] Liu, H. Key Points for Construction Quality Control of Steel Bar Concrete Structure. *Academic Journal Of Science And Technology*. **1**, 53-56 (2022)

[11] Zhao, W. Three-dimensional collapse simulation on the spatial structure of concrete assembly building based on BIM. *International Journal Of Critical Infrastructures*. **17**, 251-270 (2021)

[12] Topchiy, D., Bolotova, A., Zelentsov, A., Vorobev, A. & Atamanenko, A. Technical rationing of the construction technology of reinforced concrete floor slabs using non-removable empitness-liners. *International Journal Of Civil Engineering And Technology*. **10**, 2160-2166 (2019)

[13] Liu, C., Zhang, F. & Zhang, H. Comparative analysis of off-site precast concrete and cast-in-place concrete in low-carbon built environment. *Fresenius Environ. Bull.* **29**, 1804-1812 (2020)

[14] Park, J., Kim, D., Park, W., Kim, B. & Oh, S. Development of oil leakage stability evaluation for composite aterproofing methods using asphalt mastic and modified asphalt sheet in concrete structure. *Journal Of The Korea Institute Of Building Construction*. **19**, 19-29 (2019)

[15] Wang, L., Jiang, H., Li, Z. & Ma, G. Mechanical behaviors of 3D printed lightweight concrete structure with hollow section. *Archives Of Civil And Mechanical Engineering*. **20**, 1-17 (2020)
[16] Zhang, J. & Zhao, F. Applications of Light Steel and Light Concrete Structure System in Island Building. *Journal Of Coastal Research*. **107**, 73-76 (2020)
[17] Raval, A. & Patel, C. Development, challenges and future outlook of 3d concrete printing technology. *International Journal On Emerging Technologies*. **11**, 892-896 (2020)
[18] Putranto, R. & Ariyansyah, R. Construction method of Abila precast concrete for housing. *Jurnal Teknik-Sipil*. **22**, 70-74 (2021)
[19] Vadimovich, V., Evgenyevich, E., Vadimovich, L., Dmitrievich, Z., Berikovna, K., Ivanovna, M. & Galinurovna, G. The use of structures made of composite reinforced concrete. *Technology*. **10**, 19-25 (2019)
[20] Yamanoi, Y. & Maekawa, K. Shear bifurcation and gravelization of low-strength concrete. *Journal Of Advanced Concrete Technology*. **18**, 767-777 (2020)
[21] Lăpuşte, A. & Mociran, H. Cost benefit analysis for finding out the optimal structural rehabilitation solution of a reinforced concrete trestle bridge. *Science And Technology*. **10**, 13-20 (2021)
[22] Naser, A. A review study on theoretical comparison between time-dependent analysis models for prestressed concrete bridges. *Jurnal Kejuruteraan*. **34**, 375-385 (2022)

Edited by: Zhengyi Chai
Special issue on: Data-Driven Optimization Algorithms for Sustainable and Smart City
Received: Jan 24, 2024
Accepted: May 6, 2024